Bulletin of Volcanology (2020) 82: 49
https://doi.org/10.1007/s00445-020-01386-4

RESEARCH ARTICLE

Spatter stability: constraining accumulation rates and temperature conditions with experimental bomb morphology

E. Rader[1] · R. S. Wysocki[2] · J. Heldmann[3] · K. Harpp[4] · M. Bosselait[4] · M. Myers[5]

Received: 19 October 2019 / Accepted: 5 May 2020 / Published online: 30 May 2020

Abstract

We have developed the first experimental methodology to create a volcanic spatter pile using molten basalt. This method permits reproduction of thermal conditions that yield the wide variety of spatter morphologies observed in nature. The morphology of the clasts is most strongly controlled by the time the clast spends above the glass transition temperature, which is in turn affected by the rate of accumulation and cooling of the deposit. Also, spatter piles that remain hotter over longer durations experience increased fusion between clasts, less void space between clasts, and generally larger aspect ratios. Our experimental method successfully replicated natural microcrystal textures, rheology, and clast size. Work is still therefore required to achieve realistic vesicle distribution and deposit void space. Based on presented experimental work, we estimate emplacement conditions of Southern Idaho spatter vents to have been ~ 850–900 °C, with eruption temperatures closer to 1000–1100 °C. The rapid decrease from eruption temperature to effective emplacement temperature is the result of clast flight as well as equilibrating with the cooler surrounding material. The morphology of the natural clasts matches experiments that have accumulation rates of 2.5–4.5 m/h, which also is consistent with the few measurements made at active eruptions. Finally, we provide a constraint on the temperatures and accumulation rates that can lead to the construction of fused spatter features, as well as provide the steps for future experiments to investigate other aspects (such as compression, impact, and larger sizes) of spatter formation by adapting our methodology.

Keywords Clast welding · Basaltic cone collapse · Rheomorphism · Volcanic glass

Introduction

Spatter deposits consist of pyroclasts large and hot enough to retain some fluidity after ejection from a volcano (e.g., Sumner et al. 2005; Patrick et al. 2011; Moufti et al. 2013; Fodor and Németh 2015). They are readily identified in an outcrop by the outline of a quenched dense rind around a more vesiculated core (when fractured), or simply by their lumpy glassy exterior in outcrop (Carracedo Sanchez et al. 2012). Physical volcanology studies looking at size, shape, and temperature of smaller non-agglutinated particles (ash and lapilli) have linked these characteristics to eruptive conditions of ancient eruptions (e.g., Pyle 1989; Costantini et al. 2009; Myers et al. 2019). Yet the same practices have only recently been applied to the morphological patterns captured by the hottest of the pyroclasts, spatter bombs which suggests there is an untapped record of eruption dynamics at spatter-producing volcanoes (Jones et al. 2018; Rader et al. 2018).

A few studies have compared deposit morphology produced by basaltic volcanoes with eruptive conditions (Parcheta et al. 2012, 2013; Stovall et al. 2012; Rader et al. 2018; Jones et al. 2018). These studies focused either on vesiculation in detail, illustrating how vesicles can grow and coalesce as ascent rate slows, and a fountain decreases in height and temperature (Parcheta et al. 2012, 2013; Stovall

Editorial responsibility: L. Pioli

Electronic supplementary material The online version of this article (https://doi.org/10.1007/s00445-020-01386-4) contains supplementary material, which is available to authorized users.

✉ E. Rader
erader@uidaho.edu

[1] University of Idaho, Moscow, ID, USA
[2] Syracuse University, Syracuse, NY, USA
[3] NASA Ames, Mountain View, CA, USA
[4] Colgate University, Hamilton, NY, USA
[5] Montana State University, Bozeman, MT, USA

et al. 2012), or included the morphology of the partially fused bombs to quantify eruptive dynamics (Rader et al. 2018; Jones et al. 2018). The most thorough studies characterizing basaltic spatter deposits were completed in the Eastern Snake River Plane in Idaho (USA) and inside Hawaii Volcano National Park in Hawaii (USA). Basaltic eruptions between 7000 and 30 years old produced extensive spatter deposits in both of these locations (Kuntz et al. 1982; Stearns 1924; Parcheta et al. 2012). The ease of access and the preservation of the deposits has resulted in detailed studies of natural spatter morphology. In this study, we carry out a comparison of these natural deposits to validate and test the experiments presented in this study.

The shape and degree of welding in spatter deposits indicate that differing levels of eruption energy (in the form of accumulation rate and temperature) form the distinctive morphologies of natural deposits in relatively young and unadulterated spatter piles. For example, clasts from Idaho (USA) range in modal core vesicularity from 49 to 67% with an average of 55%, whereas clasts from Hawaii (USA) ranged from 27 to 73% with an average of 50% (Rader et al. 2018; Jones et al. 2018). These deposits also vary in how welded (F-value) and how flattened (aspect ratio) the clasts end up. The *F* value, which is simply the percentage of the perimeter of a clast that is fused to another clast, and other morphological characteristics of spatter were found to correlate experimentally with thermal conditions (Rader and Geist 2015; Rader et al. 2018). However, these experiments were small-scale and improving upon them could allow for a better understanding of emplacement conditions. Constraining how emplacement conditions control spatter morphology could provide an important tool for determining specific thermal and volatile conditions of eruptions, particularly those which were unwitnessed (e.g., Gerlach and Graeber 1985; Mouginis-Mark et al. 1992; Berman and Hartmann 2002).

Spatter clasts respond to their emplacement environment, e.g., a rapidly accumulating slope near a vigorous fountain, by deforming plastically to different extents depending on their rheological properties (Sumner et al. 2005). The rheology of a three-phase clast is controlled by four factors inherent to the magma including eruption temperature, silica content, crystal content, dissolved volatile content, and gas content which are linked strongly to the eruption dynamics as well as shallow conduit conditions (Head III and Wilson 1989; Sumner et al. 2005; Lautze and Houghton 2005; Robert et al. 2014; Gurioli et al. 2014). For an ejected clast, the emplacement environment has a strong control on the change in temperature experienced by the clast after deposition (Rader and Geist 2015; Capaccioni and Cuccoli 2005). All these factors affect the rate of cooling of the spatter pile, and thus the morphology of clasts within the deposit, as well as its annealing or fusing capacity (Rader and Geist 2015). Elevated temperatures decrease lava viscosity, allowing clasts to deform readily because clast rigidity is proportional to the temperature of the material (e.g., Webb and Dingwell 1990; Stevenson et al. 1996; Morrison et al. 2020). At hotter temperatures, clasts will more readily droop and fill in gaps, resulting in a negative correlation between the amount of void space between clasts and the thermal conditions (Giordano et al. 2005; Russell and Quane 2005; D'Oriano et al. 2013; Rader and Geist 2015). In contrast, elevated crystal content increases apparent viscosity, resulting in clasts that are more rigid and therefore less able to fill in void spaces, deform, or droop at the same temperature as clasts that have lower crystal content (Mader et al. 2013). For example, apparent viscosity for Hawaiian lava will increase an order of magnitude with only 15% crystallinity (Harris and Allen 2008; Mueller et al. 2011; Mader et al. 2013; Sehlke et al. 2014). The inclusion of crystals and vesicles in molten rock also affect heat transfer and thus the ability for spatter clasts to fuse together (Herd and Pinkerton 1997; Harris et al. 2013; Hofmeister et al. 2016). Natural bombs have vesiculated cores and thin dense rims due to bubble coalescence and growth in the insulated interior and a rapid cooling of the exterior (Herd and Pinkerton 1997; Shea et al. 2010; Stovall et al. 2012; Vanderkluysen et al. 2012; Pioli et al. 2012; Rader et al. 2018; Jones et al. 2018). Thus, crystals, vesicles, and melt must be present in spatter experiments in similar proportions and in a similar distribution to achieve realistic deposit conditions. The methods of this paper were thus designed to produce a three-phase bomb of realistic morphology and chemical composition.

Systematic changes in spatter bomb morphology suggest physical parameters of clasts are related to eruption energy and temperature primarily via accumulation rate (Rader et al. 2018; Jones et al. 2018). However, until now, no methods to experimentally study the effects of emplacement conditions on clast morphological existed. We provide a starting point for the experimental study of spatter clasts with an emphasis on accurately replicating and constraining the starting temperature and the addition of new hot material (accumulation rate) of spatter deposit formation.

Methodology

Experimental clast formation

Experiments were conducted at the Syracuse Lava Project facility at Syracuse University in Syracuse, NY (USA). The ~300 lb capacity gas-powered hydraulically tilting furnace was rebuilt after it was disposed of by a metal casting factory. Our methodology below outlines an experimental procedure that approximates a natural process (spatter formation) into components that can be manipulated in a laboratory setting. For this preliminary set of experiments, we focused on isolating the role of differing starting temperature and accumulation

rate on spatter deposit morphology. The setup of the furnace does not allow for precise control of starting temperature, gas or crystal content, or total volume of each experimental clast unlike other experimental set-ups (e.g., Quane and Russell 2005; Grunder et al. 2005; Quane et al. 2009; Wadsworth et al. 2014). Instead of having set points for these conditions, we measured them during the experiment and achieved a broad range of thermal conditions while keeping other factors consistent. Despite these challenges, this system allows for an accurate size of spatter clasts, thus eliminating heat transfer scaling issues. The end goal of this study was to produce a three-phase silicate mixture that had realistic shapes, sizes, and the degree of fusion between clasts (*F* value see Rader et al. 2018) compared with non-rheomorphic natural spatter ramparts in Idaho, USA, and Hawaii, USA, as detailed in Rader et al. (2018) and Jones et al. (2018).

The steps listed below were designed to isolate the thermal influences on spatter deposit morphology while keeping other factors (e.g., fragmentation, overburdening, heat loss from the margins of the deposit) consistent. These assumptions must be considered when extrapolating the results to natural systems. By outlining the different parts of the methodology below, future experiments can be used to make discrete steps to isolate the role of other critical factors. For example, Part 1 can be changed to include a smaller grainsize, which would result in more evenly distributed vesicles.

Part 1. Starting set-up

Basalt gravel (sieved to ~ 1 cm^3) from the Keweenaw Chengwatana Volcanic Group (Michigan, USA) is the standard starting material for the Syracuse Lava Project. Material is recycled to minimize the energy needed to induce melting and to aid in the evacuation of the crucible, thus prolonging its life (e.g., Lev et al. 2012; Edwards et al. 2013; Dietterich et al. 2015; Rumpf et al. 2018; Farrell et al. 2018; Koleszar et al. 2018; Lev et al. 2019). Chips of glassy, remelted material were heated in a 450-kg capacity tilting propane furnace for at least 48 h, to a temperature of about 1300 °C. The process of using previously melted starting material results in a near-total degassing of the molten rock and a slight chemical drift (see results and discussion for the evidence and reasoning behind this). Chemical composition of fresh starting material (gravel) and remelted material were determined by XRF (Table 1). The recycled nature of the material removes all nucleation surfaces, hindering crystal formation during cooling (Lofgren 1983). As volatiles and crystals will affect the heat capacity of a silicate melt, their inclusion in this methodology was considered critical. To achieve a three-phase system at realistic eruptive temperatures (800-1100 °C), we added cold gravel to the molten material as it exited the furnace in a ~ 1:10 ratio by weight (Fig. 1; Video 1). The addition of cold gravel serves three purposes: (1) it adds volatiles back into the melt, (2) provides nucleation sites for crystals to form, and (3) lowers the temperature of the starting material from ~ 1300 down to ~ 1100 °C which is closer to reported natural basaltic spatter temperatures.

Part 2. Clast manipulation

We used a long-handled steel paddle to mix the gravel into the molten material by folding the edges repeatedly into the middle of the mass, similar to kneading dough. Molten material and gravel were blended and manipulated for a period of time (t_{man}) to lower and homogenize the temperature of the mixture. A clast was considered formed once the outside rind was strong enough to withstand movement without dripping during transfer to the spatter pile. This endpoint was selected as a target because formed clasts mimicked the dimensions and apparent rheology of the majority of the natural spatter clasts measured in Idaho (Rader et al. 2018) and was a way to keep clast fluidity (highly temperature dependent) relatively controlled to target accumulation rate as the primary variable.

Step 3. Clast placement

The experimental spatter piles were designed to minimize the effects of surrounding thermal sources, such as insulating clasts or compression from overburdening, which causes clasts to deform more readily. While these factors are unavoidable in nature, they must be isolated and studied separately to understand the influence of each component. We controlled for these factors by constructing experimental spatter piles out of three clasts gently stacked on top of one another, thus removing the force of impact from the experiment. Clast A was placed first followed by B and C. Each pile was given a sample name (Table 2). The time between clast placements is $t_{between}$ and the time when the glass transition was achieved was t_g. We acknowledge that some thermal energy was lost out of the side of the pile to the surrounding air due to our simplification of the system.

Measurements concurrent with clast formation

Two k-type (Nickel-Chromium / Nickel-Alumel) thermocouples housed in 1 cm diameter steel sheaths were placed between clasts, one between A and B, and one between clasts B and C to measure the maximum contact temperature ($T_{contact}$) and the cooling rate of the clast interface (Table 3). As the robustness of these thermocouples prevented rapid measurements, surface temperatures were collected using Forward-Looking Infrared (FLIR T300 camera) images during the pour of the molten material and just before the clast was placed into contact with the other clasts. Error on our k-type thermocouples and FLIR camera were ± 2 °C. Several piles (SLP16–11 through 14) were documented with a second FLIR

Table 1 List of experimental spatter piles and measurements for each pile

Sample Name	Accumulation rate m/h	Total thickness cm	Aspect ratio Average of clasts	Void space %	Average clast T °C	Fusion
SLP16–05	1.9	23	0.48	6.6	620	No
SLP16–06	3.6	39	0.69	9.1	659	No
SLP16–07	3.1	24	0.29	3.2	762	No
SLP16–08	2.9	22	0.39	2.2	774	No
SLP16–10	4.2	32	0.38	1.0	776	Half
SLP16–11	3.7	21	0.31	0.9	868	Yes
SLP16–12	3.9	18	0.33	0.4	874	Yes
SLP16–13	3.4	19	0.35	0.3	883	Yes
SLP16–14	3.7	24	0.57	0.9	857	Half
SLP16–15	5.5	28	0.57	1.7	940	Yes
SLP16–16	3.9	21	0.41	0.5	884	Yes
SLP16–17	3.1	25	0.44	0.8	914	Yes
SLP16–18	6.2	22	-	5.6	-	No

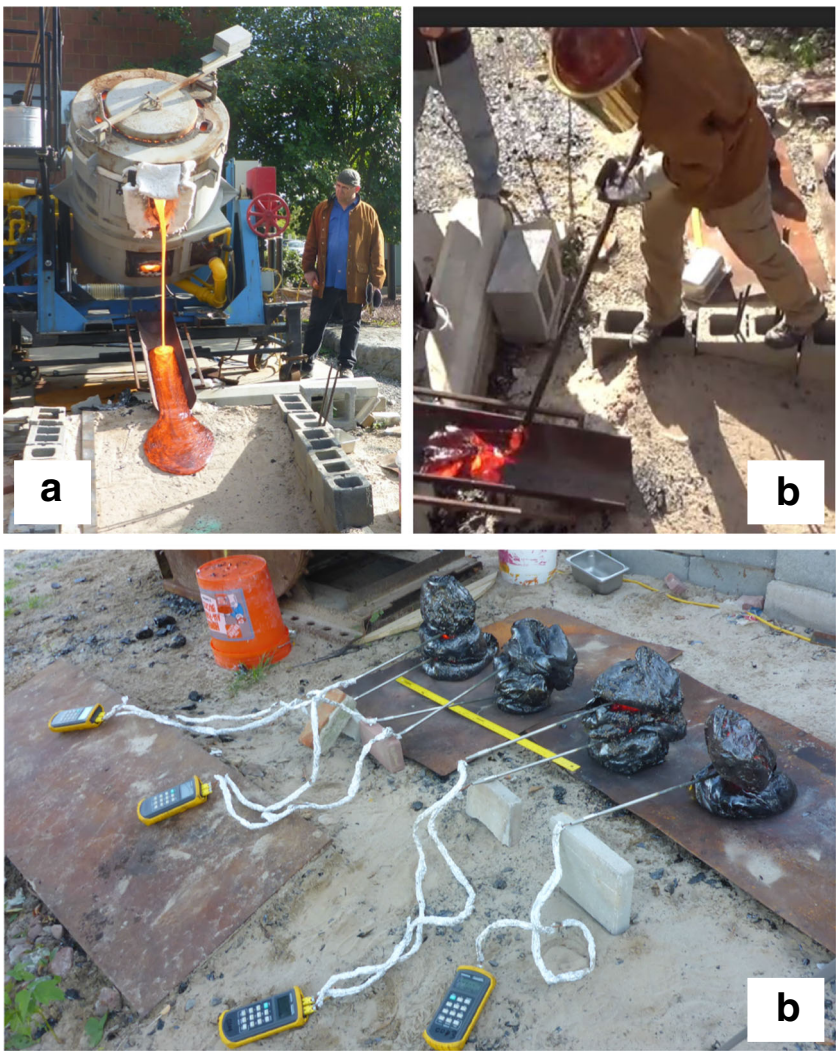

Fig. 1 **a** Molten rock of basaltic composition is poured from a hydraulic tilting furnace. **b** And then fashioned into a single clast using a metal paddle. **c** Clasts are stacked upon one another to create spatter piles. See supplemental video 1 for more details

Table 2 Normalized whole rock (WR) geochemical analysis of starting gravel and remelted material analyzed by XRF (wt. %). Precision on 41 replicate analyses of USGS Standard Reference Material BHVO-2 was <0.75%, except for K_2O (1.20% 1σ), P_2O_5 (1.28% 1σ), and Na_2O (2.41% 1σ). All major element oxides for the same BHVO-2 replicates yielded differences from known values of <0.6%, except for Na_2O (1.58%) and P_2O_5 (6.39%). Point analysis of glass and crystal phases analyzed by electron microprobe at USGS Menlo Park. Precision on 4 replicates of BHVO-2 <0.75 wt. % for all elemental oxides except CaO (0.82 wt. %) and TiO_2 (1.0 wt. %)

Sample #	Type	SiO_2	TiO_2	Al_2O_3	FeO_{tot}	MnO	MgO	CaO	Na_2O	K_2O	P_2O_5	Total
2016	[1]Remelt - WR	53.5	1.7	15.8	10.0	0.2	6.5	9.1	2.6	0.7	0.00	99.09
2015	Gravel - WR	50.4	2.0	15.1	12.7	0.2	6.5	9.3	2.7	0.8	0.22	97.93
2014	[2]Remelt	53.3	1.9	15.5	10.5	0.2	6.2	8.8	2.7	0.8	–	99.40
1	Glass	54.4	1.9	15.6	7.8	0.2	7.7	8.8	2.7	0.7	–	99.73
2	Glass	54.6	1.8	17.3	7.2	0.1	6.3	8.8	3.3	0.6	–	100.4
3	Glass	53.8	1.8	15.7	9.8	0.2	6.3	8.8	2.8	0.9	–	99.74
4	Glass	53.8	1.9	15.9	9.4	0.2	6.7	8.7	2.6	0.8	–	97.91
5	Glass	53.9	1.9	15.7	9.6	0.2	6.3	8.9	2.7	0.8	–	98.59
6	Glass	54.8	1.8	16.8	8.6	0.1	4.9	8.9	3.4	0.7	–	98.59
7	Glass	54.2	1.7	15.6	8.3	0.1	7.8	8.7	3.0	0.6	–	98.46
8	Glass	54.1	1.9	15.8	9.3	0.2	6.8	8.5	2.7	0.8	–	99.16
9	Glass	54.5	1.8	16.1	9.1	0.2	6.0	8.7	2.9	0.7	–	100.4
10	Glass	54.5	1.8	15.6	9.3	0.1	6.6	8.5	2.7	0.8	–	99.85
11	Glass	54.6	1.8	15.5	9.2	0.2	6.7	8.5	2.7	0.7	–	98.44
12	Glass	54.1	1.9	15.9	9.2	0.3	6.5	8.6	2.9	0.8	–	99.60
13	Glass	54.1	1.8	15.6	9.0	0.3	6.7	8.6	2.9	0.9	–	100.4
14	Glass	54.3	1.8	15.5	9.2	0.2	6.8	8.5	2.8	0.8	–	98.57
15	Glass	54.7	1.8	15.8	9.1	0.2	6.5	8.4	2.8	0.7	–	99.05
16	Glass	53.8	2.0	15.8	10.9	0.3	5.4	7.9	3.0	0.8	–	98.92
17	Glass	53.7	1.9	15.6	9.6	0.2	6.7	8.5	3.0	0.8	–	99.20
18	Glass	53.5	1.8	15.8	9.5	0.3	6.7	8.8	2.8	0.8	–	98.30
19	Glass	54.0	1.9	15.7	9.0	0.3	6.8	8.6	2.9	0.8	–	99.57
20	Glass	52.8	1.8	14.3	8.9	0.3	10.7	8.3	2.4	0.5	–	99.42
21	Glass	53.6	1.8	16.0	9.4	0.2	6.5	8.7	3.0	0.9	–	99.93
22	Glass	54.0	1.8	15.9	9.6	0.1	6.6	8.5	2.5	0.8	–	98.84
23	Glass	54.2	2.0	15.6	9.2	0.2	6.6	8.6	2.9	0.8	–	98.72
24	Glass	54.0	1.9	15.8	10.6	0.1	5.2	8.4	3.1	0.9	–	99.50
25	Glass	55.6	2.1	15.2	7.7	0.1	5.3	10.2	2.9	0.9	–	99.12
26	Glass w/ microlites	55.9	2.2	15.3	7.3	0.1	5.3	10.2	2.7	0.9	–	98.46
37	Glass	54.8	1.8	16.2	9.0	0.2	5.6	8.9	2.6	0.7	–	101.3
38	Glass	51.6	1.3	8.4	14.1	0.4	16.9	5.9	0.9	0.2	–	102.4
39	Glass	59.0	1.5	19.2	4.5	0.1	2.5	8.4	3.3	1.5	–	99.25
40	Glass	53.6	2.0	16.2	11.1	0.2	5.3	7.8	2.5	1.0	–	100.7
41	Glass	54.8	1.2	15.9	9.3	0.2	6.4	8.8	2.6	0.6	–	99.82
42	Glass	54.5	2.3	15.5	9.4	0.1	6.4	8.3	2.6	0.8	–	100.3
43	Glass	53.5	2.3	15.9	9.3	0.2	6.7	8.4	2.9	0.7	–	99.27
44	Glass	53.8	2.2	15.5	9.4	0.2	6.6	8.4	3.0	0.8	–	99.41
31	Cpx	50.1	1.0	1.9	14.5	0.3	14.2	17.6	0.4	0.0	–	100.7
34	Cpx	51.0	0.9	1.7	14.0	0.4	13.8	17.5	0.4	0.0	–	100.4
35	Cpx	51.6	0.8	1.3	14.7	0.4	14.1	16.6	0.3	0.0	–	101.0
36	Cpx	51.5	0.8	2.0	14.5	0.4	14.0	16.3	0.3	0.1	–	98.43
27	Fe-oxide	0.8	53.5	0.3	40.8	0.6	0.1	0.8	0.0	0.0	–	99.31
28	Fe-oxide	0.0	48.6	0.0	45.4	2.6	0.5	0.0	0.0	0.0	–	103.1
29	Fe-oxide	0.2	13.5	0.3	82.2	1.5	0.3	0.0	0.1	0.0	–	97.71
30	Fe-oxide	0.0	48.9	0.1	44.7	2.5	0.7	0.2	0.1	0.0	–	102.9
32	Plag	54.0	0.1	28.6	0.6	0.0	0.0	11.9	4.4	0.3	–	100.0
33	Plag	55.5	0.1	26.1	2.5	0.0	1.2	8.7	5.3	0.5	–	99.77

[1] From Sehlke, A., & Whittington, A. G. (2016). The viscosity of planetary tholeiitic melts: A configurational entropy model. Geochimica et Cosmochimica Acta, 191, 277-299

[2] Average of all microprobe glass analyses of remelted 2014 material

image 10–30 s after placement to measure the cooling rate of the clast exteriors ($T_{surface}$). The overall cooling rate was calculated from thermocouple data only and used the highest temperature recorded minus 700 °C divided by the time it took to cool between those temperatures with a ± 1 s error. The formation and placement of each clast was filmed, to determine the accumulation rates respectively for each pile. The accumulation rate was calculated as the total thickness of the pile (measured after total solidification) divided by the time interval between the placement of the first clast and the final clast.

Measurements after formation of spatter piles

Once clasts had cooled enough to be handled, each spatter pile was photographed and the total height measured (Table 4). Two-dimensional void space was estimated by measuring the size of the gap between the edges of the clasts without disturbing the pile and can be visualized as the angle between the clasts. Very round clasts had larger angles and a bigger gap between them, similar to two stacked spheres (e.g., SLP16–13). After photo-documentation, the pile was sequentially dismantled by hand from top to bottom. Photo images of the contact surfaces between clasts were taken, with close-ups of regions where the clasts had fused together. Length and width of each clast and proportion of fused length between clasts (F value; a 2-dimensional percentage) were recorded before the clasts were examined in cross-section. Uncertainty for F-value is estimated at 10% as the exact value can vary depending on where the cross-section is measured. The three clasts were then broken in half with a hammer to examine interior structures. The thickness of each clast, thickness of the rind, as well as the mode and size of vesicles within the clast were all subsequently measured from photos using the program ImageJ (Schneider et al. 2012). Thickness measurements were made within 2 mm and modal vesicularity was within 5%. The aspect ratio of each clast was calculated by dividing the thickness of the clast by the mean diameter. Clasts that contained voids resulting from gas bubble coalescence, recognized as being at least four times bigger than the regular vesicle population, were characterized as having large central cavities (Table 4). Since each pile had three clasts, and two interfaces between clasts, some measurements had to be averaged to be directly comparable. For example, aspect ratio ($n = 3$) and $T_{contact}$ ($n = 2$) were averaged to give a single sample a single value for aspect ratio and for $T_{contact}$.

Microanalytical analyses

A JEOL 8900 electron microprobe at the USGS Menlo Park facility was used to obtain chemical compositions of 34 glass analyses on the remelted 2016 material, as well as four iron-titanium oxide, two plagioclase, and four clinopyroxene phenocrysts taken from the gravel that was mixed into sample SLP16–15A (Table 1). Images of microstructures observed in formed clasts were collected using a Tescan VEGA3 Scanning Electron Microscope (SEM) at the same facility. Whole rock analyses of the incorporated gravel were run at Colgate University (Hamilton, USA) on a Philips PW2404 X-Ray Fluorescence (XRF) spectrometer (Table 1). Fourier Transform Infrared (FTIR) analysis of several 200–500 μm wafers of glass were conducted at the University of Oregon (Corvallis, USA). Water concentrations were calculated using the Beer-Lambert law and a material density of 2800 g/cm^3, with methods further outlined in Myers et al. (2014).

Results

We collected thermal and morphological data on thirteen experimental spatter piles (Table 2). Most of the piles are comprised of three spatter bombs, although sample SLP16–18 was only a stack of two spatter clasts. Variable conditions during clast formation included clast accumulation rate, manipulation time, volume of molten rock, and volume of solid gravel. We estimate the ratio was about 10:1 for all piles as volumes were not directly measured during the experiments. Additionally, several equipment failures and experimental error (i.e., problems with thermocouple placement, temperature loggers, record buttons, and poor lighting) led to an incomplete data set for seven out of 13 (see Tables 3 and 4).

Clast manipulation times (time that clasts were mixed with the gravel before placement) were between 29 and 76 s and the height of the final spatter piles were between 18 and 39 cm (Tables 2 and 4). The temperature of the material dropped 125–445 °C during manipulation and with the addition of gravel. Accumulation rates for all experiments varied from 1.6 to 4.5 m/h and are positively correlated with average temperature of the clasts (Fig. 2). Clasts had aspect ratios that ranged from 0.23 to 0.95. The amount of fusion between clasts (F values) in the experiments varied widely, from 0 to 63%. The F value was identified as regions where clasts fused together and broke when being pulled apart. Typically, this resulted in shards of one bomb remaining stuck to the other after separation. Fusion was only achieved in experiments with a minimum temperature of 775 °C and at least 30 min above the glass transition temperature (Fig. 3). Interior cooling rates for all clasts ranged from 6.2 to 14.9 °C/min. Spatter bombs only fused when three conditions were met. First, the spatter clast temperatures were greater than 800 °C (Fig. 4). Second, accumulation rates were greater than 4 m/s (Fig. 4). Third, the temperature was above the glass transition for greater than 30 min ($t_g > 30$ Fig. 5).

Crystallinity and vesiculation

Out of all the clasts which fused (F value > 0%) to another clast, only sample SLP16–08 showed no signs of microcrystallization. Regions of crystallization were identified with the naked eye when samples were disassembled. These regions appeared to have a matte luster instead of the strongly glassy texture of rapidly quenched experimental material (Fig. 5a). The presence of clinopyroxene microlites was later confirmed by backscatter SEM (Fig. 5b). Crystallization was not limited to the regions of contact between clasts and was often found inside the cores of clasts, including some of those that did not fuse (SLP16–07 and 17). Images collected by SEM indicate that microlites nucleated on gravel margins and that phenocrysts from the gravel began to break down during heating, releasing gas into the clast that then formed

Table 3 Experimental parameters for inter-clast contacts of spatter piles

Experiment	Microlites	F-value %	Cooling rate °C/min	$T_{contact}$ °C	$T_{surface}$ °C	$t_{between}$ s	t_g s	Aspect atio 2-clast average	Notes
SLP16–05 AB	No	0	12.3	601	550	375	0	0.47	–
SLP16–05 BC	No	0	14.9	580	690	270	0	0.43	–
SLP16–06 AB	No	0	–	–	585	230	–	0.73	Temperature logger malfunction
SLP16–06 BC	No	0	–	–	734	210	–	0.66	Temperature logger malfunction
SLP16–07 AB	No	0	6.5	818	755	110	24	0.31	–
SLP16–07 BC	No	0	11.0	833	770	170	17	0.42	–
SLP16–08 AB	No	0	6.5	837	776	120	30	0.29	–
SLP16–08 BC	No	0	7.9	703	772	145	2	0.28	–
SLP16–10 AB	No	9	–	–	–	135	–	0.36	Poor thermocouple contact
SLP16–10 BC	No	0	9.1	803	776	130	17	0.33	–
SLP16–11 AB	Yes	35	7.0	1009	893	88	53	0.42	–
SLP16–11 BC	Yes	20	7.8	975	843	112	42	0.41	–
SLP16–12 AB	Yes	31	6.6	1018	880	72	62	0.65	–
SLP16–12 BC	Yes	64	7.9	1080	868	91	67	0.39	–
SLP16–13 AB	Yes	16	–	–	871	97	–	0.31	Temperature logger malfunction
SLP16–13 BC	Yes	31	7.7	1100	895	111	55	0.36	–
SLP16–14 AB	Yes	24	8.2	1035	856	125	53	0.66	–
SLP16–14 BC	Yes	0	8.3	837	858	104	22	0.38	–
SLP16–15 AB	Yes	27	7.2	1009	901	126	53	0.33	–
SLP16–15 BC	Yes	–	9.2	1016	978	120	42	–	Abnormal clast placement of clast C
SLP16–16 AB	Yes	20	6.4	1018	884	100	55	0.32	–
SLP16–16 BC	Yes	–	–	–	844	100	–	0.43	Poor thermocouple contact
SLP16–17 AB	Yes	21	7.7	983	906	129	44	0.42	–
SLP16–17 BC	No	10	–	–	921	173	–	0.39	Poor thermocouple contact
SLP16–18 AB	No	0	13.1	991	804	129	21	0.37	–

A are the lowermost clasts in a pile, whereas C is the uppermost. Data with the suffix "AB" represent conditions recorded between clast A and B. Variables include: presence of microlites; *F* value = the degree (%) of fusion between clasts; cooling rate = ($T_{contact}$ 700 °C/t_g time at $T_{contact}$); $T_{contact}$ = highest temperature recorded by a thermocouple placed between clasts; $T_{surface}$ Temperature of clast surface at time of placement; $t_{between}$ time between clast placement; t_g time a contact spent above the glass transition temperature (estimated to be 700 °C); aspect ratio (thickness of clast/longest axis). Notes include explanations for incomplete data sets

vesicles (Fig. 6). Crystal textures indicated rapid growth, though they never grew larger than ~ 50 μm, giving the rock a pilotassitic texture. Chemical compositions of the glassy and microlite-filled regions of SLP16–15A were determined by microprobe. Glass compositions match whole-rock analyses of remelted starting material but differ slightly from the fresh gravel (Table 1). Remelted material has higher SiO_2 and lower FeO contents compared with the fresh gravel (~ 54 wt.% SiO_2 in experimental recycled material compared with ~ 49 wt.% in fresh rock; ~ 9 wt.% FeO in recycled glass and ~ 12 wt.% in fresh rock). Natural clasts can also be "recycled"; however, since the predominant process altering the chemical composition is degradation of the crucible, it is not thought to be representative of a natural process that would be affecting recycled volcanic bombs (e.g., Gurioli et al. 2014; Pioli et al. 2012; Parcheta et al. 2012).

Without gravel mixed in, there were no vesicles and FTIR analysis of the glass contained between 67 and 105 ppm H_2O, which is approaching the detection limit of the method. However, the incorporation of gravel into the molten material caused experimental clasts to contain vesicles (Fig. 7a). Although some gas escaped through bubble bursts, much of the gas can be seen as vesicles in the cold clasts. Two thirds of the clasts contained a central cavity (large gas pocket; Fig. 7b), and modal percentage of vesiculation in the core varied between 10 and 70%, where the average value of modal vesicularity in all clasts was 30%.

Degree of fusion, aspect ratio, and void space

Certain characteristics (*F* value and aspect ratio) generally increased with increasing temperature and/or time, t_g, spent

Table 4 Physical characteristics of each experimental clast

Sample	Microlites	Vesicle measurements							Initial surface cooling rate	Notes
		Core mode	Core size	Rind mode	Rind thickness	Central cavity	Aspect ratio	t_{man}		
		%	mm	%	mm			s	°C/min	
SLP16–05 A	No	30	3	5	1	0	0.56	50	–	–
SLP16–05 B	No	–	–	–	–	–	0.37	70	–	Poor imagery
SLP16–05 C	No	–	–	–	–	–	0.50	40	–	Poor imagery
SLP16–06 A	No	25	8	1	3	0	0.73	33	–	–
SLP16–06 B	No	–	–	–	–	0	0.72	60	–	Poor imagery
SLP16–06 C	No	–	–	–	–	0	0.60	60	–	Poor imagery
SLP16–07 A	No	35	54	1	2	1	0.29	55	–	–
SLP16–07 B	No	10	7	0	2	1	0.33	40	–	–
SLP16–07 C	No	–	–	–	–	0.5	0.23	50	–	Poor imagery
SLP16–08 A	No	70	10	5	10	1	0.33	55	–	–
SLP16–08 B	No	30	50	2	8	1	0.42	55	–	–
SLP16–08 C	No	35	30	2	2	1	0.43	45	–	–
SLP16–10 A	No	45	30	5	8	1	0.38	63	180	–
SLP16–10 B	No	35	15	1	2	1	0.28	62	–	–
SLP16–10 C	No	–	–	–	–	0.5	0.48	65	–	Poor imagery
SLP16–11 A	Yes	25	30	10	12	0	0.23	76	–	–
SLP16–11 B	Yes	20	10	2	4	1	0.35	43	–	–
SLP16–11 C	Yes	35	20	1	8	0	0.36	48	–	–
SLP16–12 A	Yes	35	12	5	3	1	0.38	36	–	–
SLP16–12 B	Yes	25	13	10	2	0	0.28	36	140	–
SLP16–12 C	Yes	15	5	0	1	0	0.35	40	–	–
SLP16–13 A	Yes	15	10	10	10	0	0.41	39	–	–
SLP16–13 B	Yes	30	32	0	1	1	0.40	34	130	–
SLP16–13 C	Yes	20	8	30	8	1	0.24	36	–	–
SLP16–14 A	Yes	20	15	1	11	1	0.40	42	170	–
SLP16–14 B	Yes	20	11	0	2	1	0.65	57	–	–
SLP16–14 C	Yes	45	25	0	1	1	0.67	45	–	–
SLP16–15 A	Yes	15	15	15	10	1	0.32	42	–	–
SLP16–15 B	Yes	25	6	10	5	0	0.35	50	–	–
SLP16–15 C	Yes	35	16	15	3	1	–	43	–	Abnormal clast placement
SLP16–16 A	Yes	20	12	1	2	1	0.36	29	150	–
SLP16–16 B	Yes	25	7	20	3	0.5	0.37	40	–	–
SLP16–16 C	Yes	30	25	5	2	1	0.50	46	–	–
SLP16–17 A	Yes	25	9	5	6	1	0.52	46	–	–
SLP16–17 B	Yes	30	12	0	1	1	0.31	49	–	–
SLP16–17 C	No	30	6	0	1	1	0.48	49	–	–
SLP16–18 A	Yes	35	10	8	11	1	0.31	68	–	–
SLP16–18 B	No	60	25	1	3	1	0.61	60	–	–

A clast with a obvious central cavity was given a value of 1, whereas a clast with no cavity was given a value of 0. Some clasts contained a smaller cavity that only occupied a part of the clast and were given a value of 0.5. The surface cooling rate was calculated using two FLIR images taken of the same clast after ~ 10 or 20 s of cooling. The variable t_{man} was the amount of time each clast was manipulated and mixed

above the glass transitions temperature (700 °C, based on measurements done by Sehlke and Whittington 2016; Fig. 4). Fusion required a minimum temperature of 775 °C and at least 30 min above the glass transition temperature. The amount of fusion between clasts (*F* values) in the experiments varied from 0 to 63%. Fused clasts had aspect ratios that

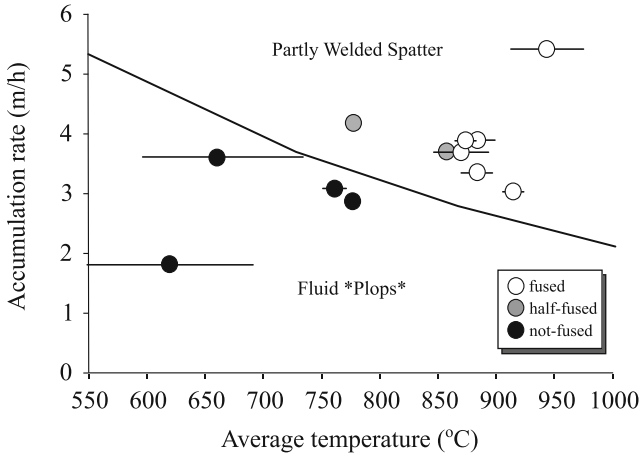

Fig. 2 Spatter piles with faster accumulation rates tended to have higher average temperature upon emplacement as well as have fusion between all three clasts (white circles). Higher accumulation rates, but lower temperature resulted in fusion between 1 or 2 clasts (gray) and the lowest rates and temperatures resulted in totally un-fused clasts (black). The black line separates two regimes named in Head III and Wilson (1989). Error bars are 1σ and are sometimes smaller than the symbols

ranged from 0.23 to 0.95. Experimental aspect ratios and void space estimates correlate negatively to higher temperatures and longer t_g (Fig. 4). Despite our attempts to minimize the effects of impact on spatter, one clast was pushed into the top of the pile as opposed to gently placed. This resulted in an anomalously high degree of fusion and so we have excluded sample SLP16–15C from our analysis (Tables 3 and 4). Void space between clasts showed little variation, ranging between 0.2 and 9%.

Texture, luster, and surface color

The texture of the outer layer of the experimental clasts can exhibit brittle features such as tears (Fig. 8a), as well as ductile

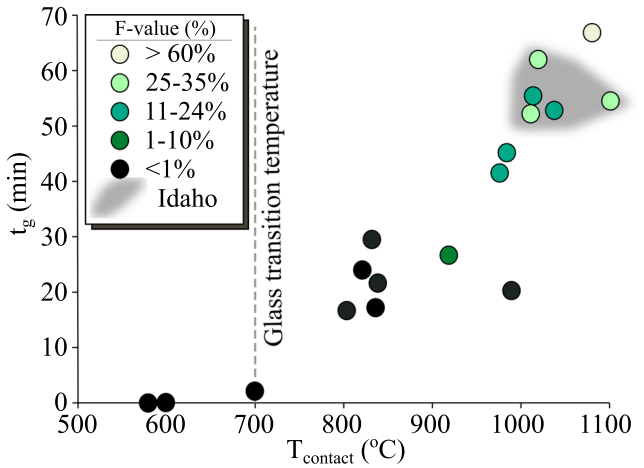

Fig. 3 The amount of fusion between two clasts is shown by the shade of green (light indicating high F value). Higher temperatures captured by thermocouple along the margin of clasts ($T_{contact}$) and greater time above the glass transition (t_g) result in greater fusion. The gray field is the range of F values measured from natural clasts from Southern Idaho (data from Rader et al. 2018). Error bars (1σ) are smaller than the symbols

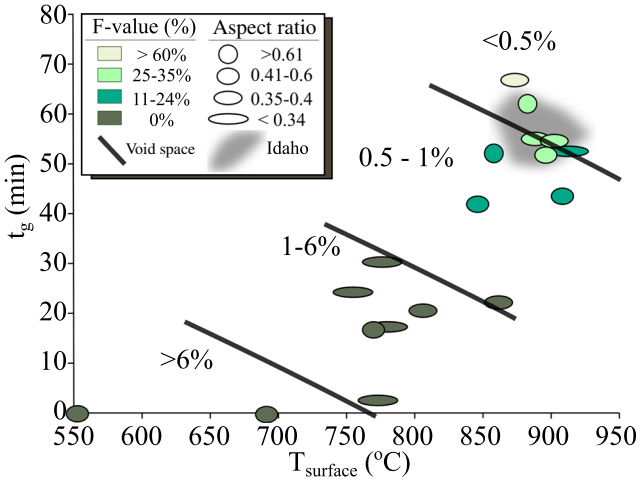

Fig. 4 Diagram showing how morphological patterns relate to surface temperature measured by FLIR and time above the glass transition temperature (t_g) in experimental spatter piles. The aspect ratio (more oblate symbols for flatter clasts), void space (fields separated by dark black lines with percentage ranges listed), and F value (lighter shades of green indicate more fusion) are represented for each experiment. Idaho spatter deposits (gray field from Rader et al. 2018) share similar F values with some experiments. Uncertainty for each of these measurements is discussed in the methods and error bars (1σ) are smaller than the symbols for the axes of the graph

features, including stretched vesicles and small-scale folds or wrinkles. Virtually all clasts had an initial colorful, shiny coating on interior and exterior surfaces that tended to dull slightly after a few hours (Fig. 8b). This coating appears different than the optical effect (iridescence) seen on fresh glassy surfaces as it is only visible on outer surfaces. A slight dulling of the luster occurs after an hour or so but has not degraded further after 4 years of storage in a dry climate. Observed clasts colors include blue, green, and gold and can occur in the same region of a sample. Only few cases of red occur in the experimental clasts (e.g., SLP16–15A-B), but only at the margin of the bombs without permeation through the clast (Fig. 8c).

Discussion

Limitations of this model and furnace

The experiments published in this manuscript provide a proof-of-concept that molten rock can be used to simulate fragmented basaltic morphologies. Below we discuss the areas which can be directly compared with natural samples and highlight those which are merely illustrative of the potential contributions that this analog model can make in the future. Additionally, we discuss the ranges of natural observations from spatter deposits to illustrate the similarities and difference with our experiments. All types of models (conceptual, numerical, analog) contain simplifications and this model is no exception. For example, by manipulating the rock to lower and more consistent

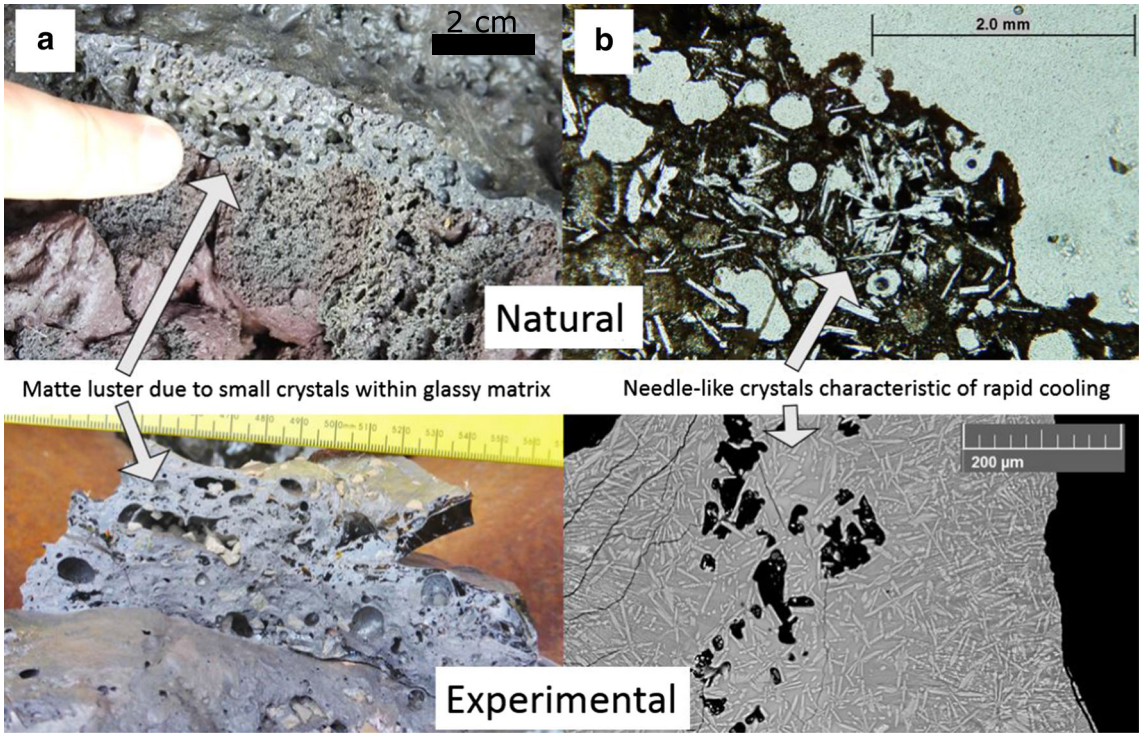

Fig. 5 Surface luster (a) in natural (top) and experimental (bottom) clasts both have a matte luster with the addition of nucleation points in the experimental material. Needle-like crystal structures are common in thin sections of natural spatter (b, top) and are mimicked on a smaller scale in SEM images of experimental spatter (b, bottom)

temperatures in order to simulate a realistic rheology, we introduce biases into other areas of the experiment. These inaccuracies and how we dealt with them are discussed below. In general, we attempted to control for these biases by making them as consistent as possible between each clast formation, thus isolating the key parameters of the study.

The experimental methods listed here are reproducible; however, recreating an experiment exactly would be difficult due to the challenges of precisely replicating the exact molten volume and proportion of gravel. While measuring gravel out before hand is possible, it is not always completely enveloped in the molten material nor is the furnace capable of depositing an exact volume into the trough. However, the results of numerous experiments done in the manner presented here, we believe, are reproduceable. The furnace exerts some undesirable influences on the experiments as well. The need to keep the material highly fluid to help it exit the furnace results in a gasless, crystal-free superheated liquid which quickly becomes an undercooled glass when exposed to the atmosphere. Furthermore, the recycling of material to aid in melting causes a drift in the chemical composition as iron oxidizes and collects as slag at the base of the crucible. The increase is SiO_2 likely results from disintegration of the silica carbide (CSi) crucible (Soldati et al. 2018). We have addressed all these issues by adding the cold, fresh gravel. In the future, by adding smaller grain sizes of fresh material, we can achieve a more homogenous mixture. Additionally, modifications to the trough where the molten material is first poured out of the furnace may allow us to determine the mass of lava and the added mass from fresh gravel in each experiment. This will help us further constrain the thermal and volatile inputs in subsequent experiments.

Thermal conditions that produce fused spatter

Previous studies identified two variables thought to control spatter welding: (a) the input of thermal energy expressed as accumulation rate; and (b) the loss of thermal energy expressed as cooling rate (Head III and Wilson 1989; Sumner et al. 2005). These metrics have been singled out because they capture the average thermal conditions of an eruption. For instance, spatter cones generally grow more rapidly (i.e., faster accumulation rate), but have slower cooling rates than cinder cone deposits (Sumner et al. 2005). The lack of fusion in cider cone deposits is generally attributed to this distinction but could also be due to an eruption temperature below the glass transition. It is important to quantify the relationship between the extent of welding and both accumulation and cooling rates, to generate a quantitative method for studying historical deposits.

Our experiments indicate that accumulation rate correlates strongly with all measures of temperature of the clasts ($T_{surface}$, $T_{contact}$, or $T_{average}$) as well as t_g, the time spent above the glass transition. By recording where and when fusion occurs (F

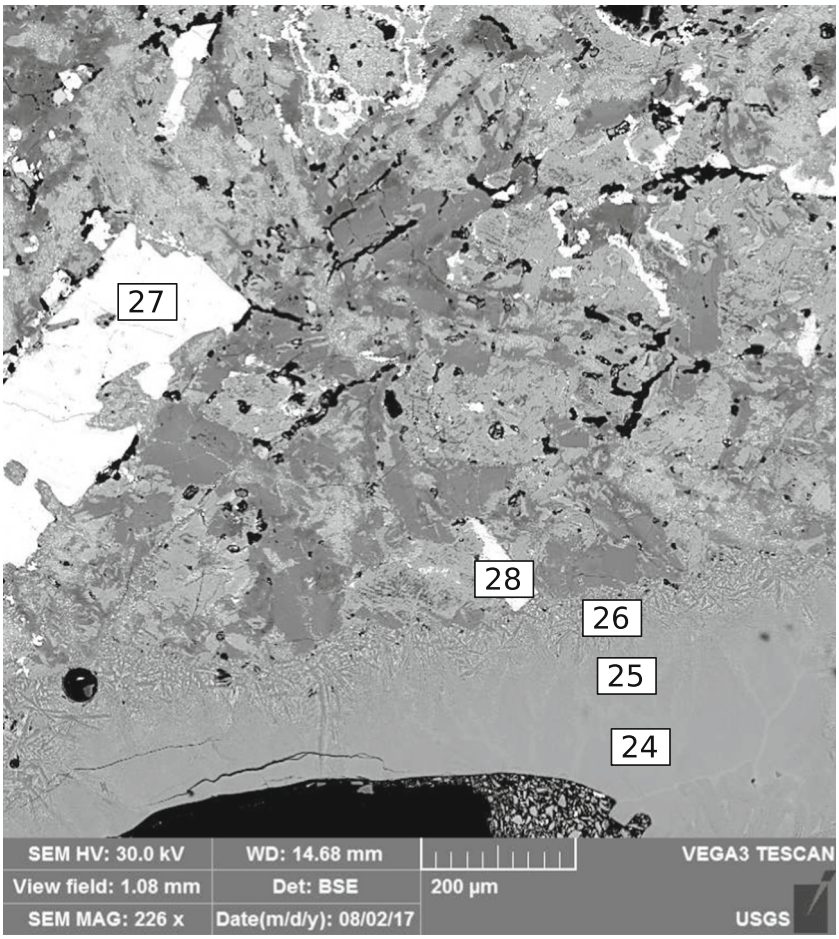

Fig. 6 SEM image of the margin between a dissolving holocrystalline piece of gravel (upper part of image) and the glassy remelted material. Microlites can be seen nucleating on the margin, located at microprobe analysis 26. Analyses 27 and 28 are of iron oxide crystals within the mixed-in gravel (upper portion of image) whereas analyses 24 and 25 are of the remelted glass

value > 0), we can constrain the thermal conditions where spatter deposits may form. Spatter bombs fused when clast temperatures > 800 °C, accumulation rates > 4 m/s, and t_g > 30 min. Also, increasing either temperature or time above the glass transition point resulted in higher F values; however, at F value > 10%, this relationship becomes less defined indicating there may be another variable we did not examine. This may be an outcome of the simplification of a three-clast pile resulting in the loss of more heat out of their sides than would natural deposits.

The cooling rate is not as well-correlated with temperature because higher initial temperatures result in faster cooling rates due to radiative cooling (e.g., Keszthelyi and Denlinger 1996; Hon et al. 1994; Oppenheimer 1991). This is opposite to the relationship proposed by Head III and Wilson (1989) and illustrates a problem with using cooling rate to compare our experiments with the natural samples. This can be seen in the wide spread of cooling rates that can result in fusion or lack of fusion in Fig. 9. The time it takes a deposit to cool is a useful measure when conceptualizing spatter deposits, as it summarizes time and temperature for a whole feature (spatter cone or cinder cone), but the actual cooling rate is highly influenced by the starting temperature of the molten rock (Ganci et al. 2012; Patrick et al. 2004). Instead of using cooling rate to represent the thermal history of the experiments, we use t_g, and the temperature of the clast upon placement ($T_{contact}$; Table 3). These two measures correlate with the F value substantially better than cooling rate, and therefore we consider them to be better indicators of the thermal history of the experiments. This concept agrees with other experimental studies on welding in volcanic deposits (e.g., Giordano et al. 2005; Russell and Quane 2005; Grunder and Russell 2005). It should be noted here that cooling and accumulation rates cannot explain the magnitude of fusion within our dataset completely, especially at higher F value, but they do allow for a set of minimum conditions to be identified (Fig. 9).

It should also be stated that a single experiment indicated compaction and impact during clast placement is certainly important for fusion between clasts as well. The high F value of experiment SLP16–15C suggests that loading from above will increase the F value irrespectively of the thermal conditions and will be explored in future experiments. Observations from footage of spatter suggest that clasts may rupture upon

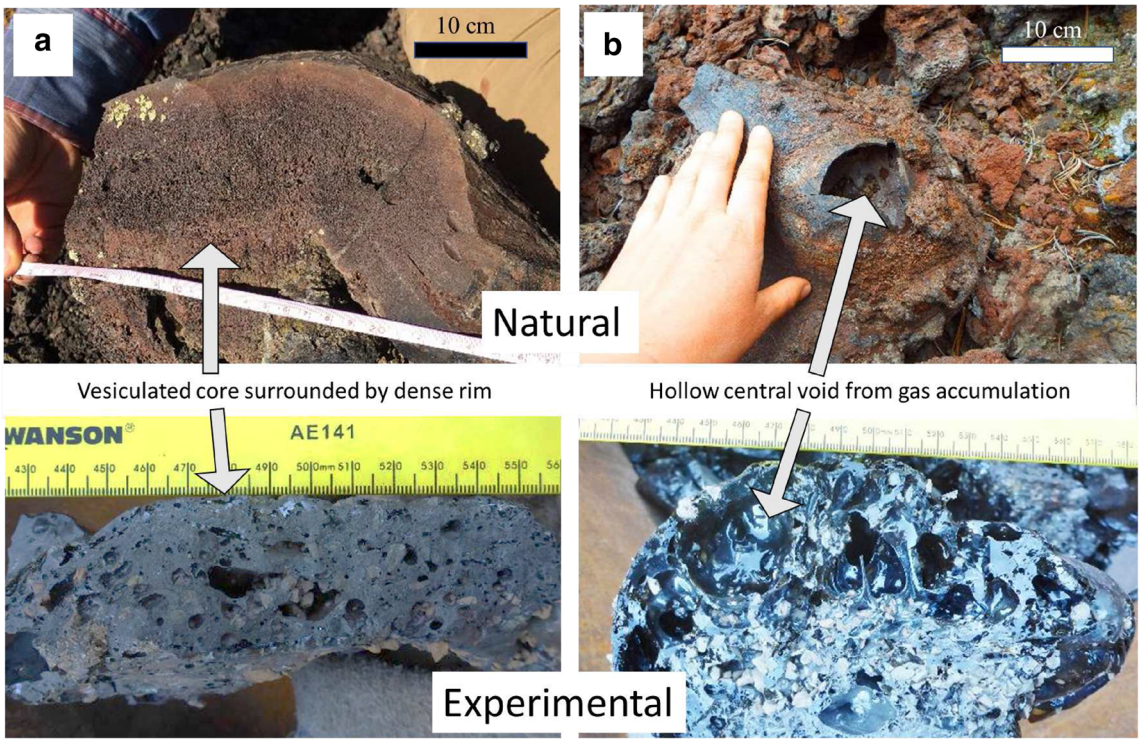

Fig. 7 Vesicle distribution in natural clasts (a, top) show the typical more vesiculated core and less vesiculated rim characteristic of spatter bombs. While we were able to generate a broadly similar pattern in experimental spatter (a, bottom), vesicles tended to be larger, more uneven, and more heterogeneous in distribution. Large central voids showing the coalescence of gas (b) in natural (top) and experimental clasts (bottom)

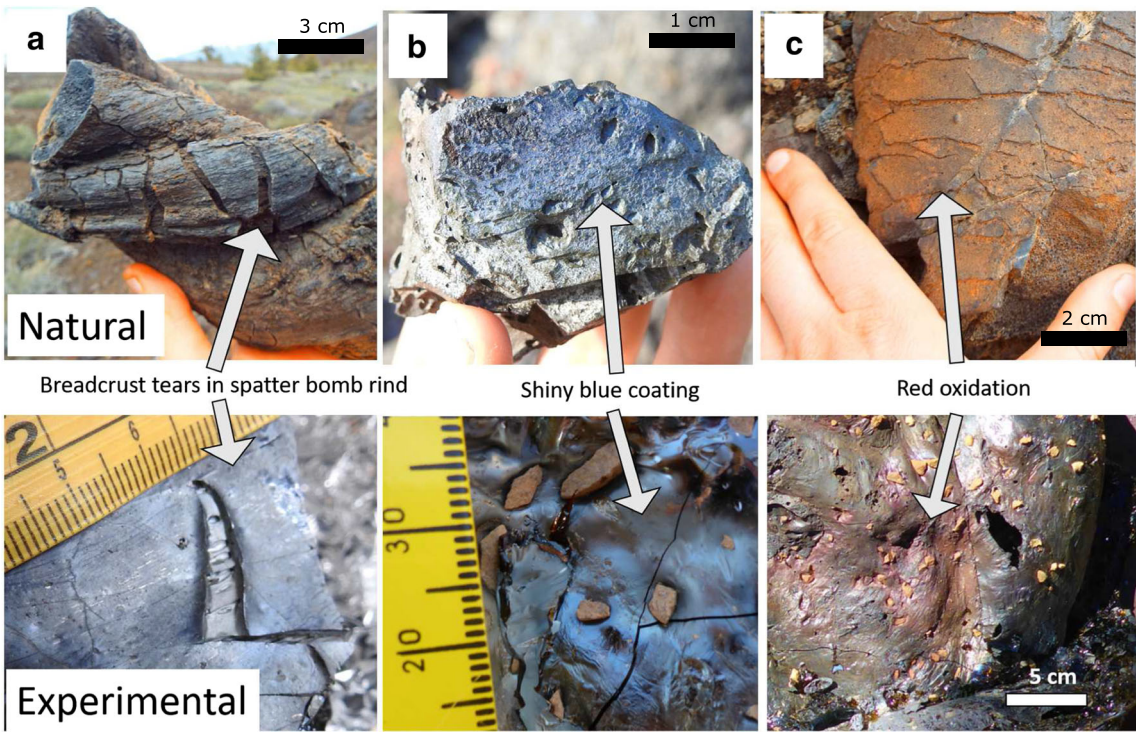

Fig. 8 Brittle crustal tears in natural clasts (a, top) and in experimental spatter (a, bottom) while still exhibiting ductile behavior due to the molten core. (b) a shiny blue coating in natural (top) and experimental clasts (bottom). (c) Red oxidation is common on natural spatter but was uncommon in experiments

impact, land extremely softly as they barely clear the top of the rampart, or even roll downhill slightly before becoming lodged; however, these accounts are not well documented in the literature. This lack of data argues for the need to investigate the role of impact in experiments as well as more thermal and velocity observations of spatter clasts on impact during active eruptions, similar to those that have been made at Stromboli but with an emphasis on how and when spatter bombs land (Worden et al. 2014; Taddeucci et al. 2012).

Temperature

Experimental spatter had measured surface temperatures ($T_{surface}$) measured at 850–900 °C and contact temperatures of 1000–1100 °C. The $T_{surface}$ values are slightly higher than measurements of the temperature when natural Hawaiian pahoehoe breakout lobes lava develops a skin (800–850 °C; Carling et al. 2015; Pinkerton et al. 2002; Hon et al. 1994). Further, the $T_{contact}$ values are consistent with temperatures of ~ 1000–1150 °C measured on newly spattered lava from Erta Ale lava lake before the lava cooled and formed the outer rind of a bomb (Carling et al. 2015). Other fountain measurements on Hawai'i lava eruptions are ~ 100 °C higher than our $T_{contact}$, which is likely because they represent maximum readings from the hottest part of lava fountains which typically fell back into the fountain (Helz et al. 1995; Vanderkluysen et al. 2012; Stovall et al. 2012).

A survey of natural spatter clasts at volcanic fields in Southern Idaho reveals a consistent range of F-values for primary vent spatter of about 31–44% (Rader et al. 2018) (Fig. 10). By overlaying F values on results from the experimental clasts, we can provide a first order constraint to thermal conditions of emplacement (Fig. 4). The experimental clasts likely cool slightly faster than natural clasts since they are not thermally insulated by surrounding clasts, so these results should be thought of as a high-cooling rate endmember. With more insulation, natural clasts likely need not achieve as high of initial temperatures to have t_g equal to those which produced realistic F values.

Accumulation rates

Spatter piles where both clasts exhibited fused textures always had an accumulation rate above ~ 2.5 m/h and spanned the range of previously denoted categories "fluid plops" and "partly welded spatter" in Head and Wilson (1989; Fig. 2). The range of accumulation rates of fusion between spatter clasts ranged from 3 to 5.5 m/h which is within the range of the few accumulation rate observations that have been made (0.6–10 m/h). The high end of this range of 10 m/h was estimated on a spatter deposit that collapsed into a clastogenic flow in Japan (Sumner 1998). The low end is constrained by

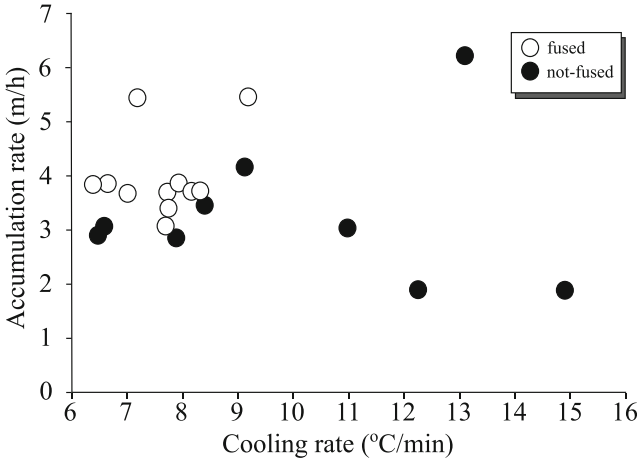

Fig. 9 Relationship of accumulation rate and cooling rate to unfused (black circles) and fused (white circles) experiments showing that accumulation rates higher than ~ 3 m/h and cooling rates < 10 °C/min allow for clast fusion in the absence of pressure or increased ambient temperature. Overlapping of clasts near this boundary reflects the precision of this method in which all variables can be difficult to hold constant. Error bars (1σ) are smaller than the symbols for time and temperature whereas F value has an uncertainty estimated at 10%

a small spatter feature erupted during the 2018 eruption at Leilani Estates (HVO eruption chronology website n.d.). Fissure 11 was reported by Hawaii Civil Defense to only be active for ~ 3 h and ultimately produced an ~ 2-m high rampart, yielding a minimum accumulation rate of 0.66 m/h (Hawaii Civil Defense Map n.d.). Given this wide range and minimal data, it is apparent that measurements of natural accumulation rates of spatter deposits are lacking.

Using the calculated accumulation rates associated with F values similar to natural deposits, we can calculate construction times for these features. The spatter cones where F value was measured vary in height (base to rim) from 1.5 m (Creon's Cave region, Idaho, USA) to 4 m (Vermillion Chasm, Idaho, USA) which give a formation time of ~ 50 min to 2.6 h (Rader et al. 2018). As all of these features involve no rheomorphic behavior, we can assume that accumulation rates must be faster than 5.5 m/h to result in collapse or flow of spatter features. It is probable, however, that the surrounding heat of larger spatter features (when compared with the 3-clast experimental pile) will allow for longer t_g at lower accumulation rates and thereby our estimates may be too large.

Aspect ratios and void space

Experimental clast aspect ratios and void space estimates correlate negatively to higher emplacement temperatures and longer t_g (Fig. 4), a pattern described as densifying and flattening by additional experiments on welding processes (Grunder and Russell 2005; Rader and Geist 2015). The range for our experimental clasts of 0.29–0.69 (Table 2) overlap with average

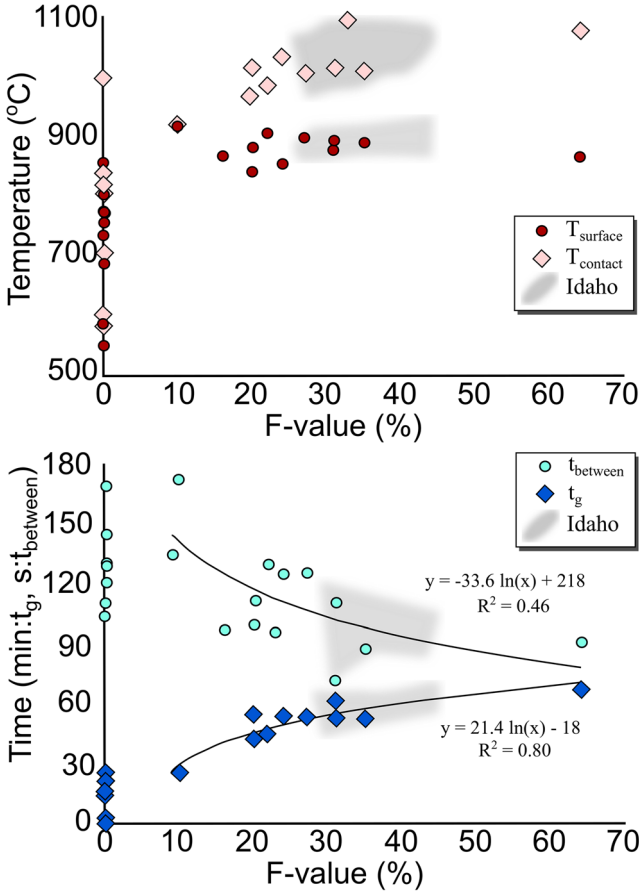

Fig. 10 Time and temperature conditions for all experiments with a range of Idaho F-values in the grey field from Rader et al. (2018). In the upper plot, light pink diamonds are the temperature between two clasts recorded with a thermocouple ($T_{contact}$), whereas dark red circles are surface temperature of the clasts shortly before placement as measured by a FLIR. Dark blue diamonds are the minutes spent above 700 °C, and the teal circles are the seconds between clast placements ($t_{between}$). Natural clasts from Idaho are in the gray field

aspect ratios for Southern Idaho spatter outcrops (0.20–0.49) and Icelandic spatter clasts (0.1–0.5) (Rader et al. 2018; Reynolds et al. 2016), indicating that we are accurately recreating aspect ratio in spatter clasts. In contrast, the void space calculations for these experiments were an order of magnitude lower than what is observed in Southern Idaho spatter, which are around 10–15% void space. The higher void space volumes in natural samples compared with our experiments are a ramification of our experimental method, in which a single clast was placed directly upon another single clast. Because experimental piles contain a maximum of three clasts, only gaps along the margin of the clasts were measured, resulting in lower void space percentages than would likely occur if we transitioned to larger experimental piles. Despite void space in experimental deposits not being directly comparable with void space estimates in natural deposits, the correlation between experimental thermal conditions and void remains negative (Fig. 4). Future experiments that involve more overlapping clasts will be required to quantify the relationship between emplacement conditions and amount of void space in a spatter deposit.

Our method of transporting clasts using tongs influenced the shape of the clast during transport. Clasts tended to droop after they were picked up, as well as inflate as gas expanded inside the clast. Drooping and inflation affected the aspect ratio of clasts, but in an unsystematic way, resulting in the variability observed in the relationship between clast aspect ratio and temperature (Fig. 4). Natural clasts also deform during transport, but typically that deformation is uniform flattening (Sumner et al. 2005). A much larger experimental and natural data set is required to turn the qualitative relationship between temperature and clast aspect ratio into a quantitative indicator of temperature range.

Vesicularities

Volatiles were initially stored in the minerals contained in the gravel, which were then released during incorporation into the molten material due to the high temperatures. Even though we were able to broadly recreate the pattern of more highly vesiculated cores (Fig. 7a), the vesicles in the experimental clasts were not as small or as evenly distributed as those in natural clasts. Vesicle walls also tended to be thicker in the experiments, leading to lower modal percentages of vesicles than is observed in natural spatter clasts and tephra produced from fountaining (Mangan and Cashman 1996; Stovall et al. 2012; Parcheta et al. 2013; Rader et al. 2018; Jones et al. 2018). On average, experimental clasts contained a little more than half as many vesicles as natural spatter. Experimental clasts had a few clasts with extreme values (10 and 70% vesiculation); however, the average value was 30%, indicating that the experimental clasts are more dense than natural clasts. We infer that this discrepancy is due to the origin of the gas in the experimental clasts, which is released from the gravel and therefore concentrated around the gravel margins. In natural clasts, magmatic gas is exsolved uniformly from a more homogeneous melt (Cashman and Mangan 1994).

Other vesiculation patterns observed in nature are reproduced in the experimental clasts. In the event of total coalescence of the vesicles in the interior, both experiments and natural clasts concentrated gas in large voids at the center or near the top of the clast (Fig. 7b). In natural deposits, hollow cores are often associated with primary vent spatter deposits, but not spatter deposits located at more distal locations (Rader et al. 2018). In contrast, the hollow interiors were common in our experiments, and their prevalence did not depend on formation conditions. We conclude that, in nature, the gas creating a hollow core might be lost during transport or after rupturing upon impact. Alternatively, it could be lost during transport down a flow, if lava is the source of the secondary spattering. Here, however, there is no post-emplacement movement that would allow for gas escape.

The lower vesicularity in experiments could have an effect on the heat transfer throughout the clast pile, as well as the ability for the clasts to deform after placement. Thermal conductivities for vesiculated basalt suggest that the difference in porosities could result in dense experimental clasts cooling as much as twice as fast as more porous natural samples (Robertson and Peck 1974). However, measurements of pahoehoe flow lobes indicate that denser samples (23%) cooled slower than moderately vesiculated (54%) flows (Keszthelyi 1994). Vesicles can also strongly affect the rheology, and subsequently the ability of clasts to droop and spread laterally (e.g., Wilson and Head 1989; Manga et al. 1998; Rust and Manga 2002). We could not document the lateral deformation of clasts in our experiment, however, because the transport by tong method had a much larger effect on the aspect ratio than subsequent deformation.

Our ability to control the amount of gas in the spatter experiments remains a weakness in our method. Even though we were able to add gas and produce vesicles in our experiments, the volume of gas was difficult to measure because different volumes of gravel were incorporated in each trial, and to differing degrees for each clast within each trial. Additionally, during manipulation, sometimes clasts would generate bubbles, allowing gas to escape, and sometimes pockets of air would be entrapped during the folding process. In future experiments, we intend to mitigate this factor by using more fine-grained starting material that can be more easily incorporated into the clast.

Crystal content and cooling rates

Very small microlites (50 μm) aligned in bands in the experimental clasts resembled textures in sheared rhyolites and welded ignimbrites (Manley 1996). Bands could have formed from shearing or folding during the manipulation process used to mix the gravel into the molten material. This differs from natural clasts which more frequently have a fairly uniform distribution of microlites increasing closer to the core, which is a pattern seen in spatter free from extensive recycling and shallow magma mixing (Rader et al. 2018; Gurioli et al. 2014). Natural spatter is relatively glassy, though phenocrysts are usually present and quench rates are not fast enough to prevent microlite growth in the interior (e.g., Cashman 1993; Lesher et al. 1999; Hort and Gardner 2000; Conte et al. 2006). In our experiments, we achieved interior cooling rates of 6.5–14.9 °C/min and initial exterior cooling rates of 130–180 °C/min in the first 10–30 s after placement. These values are comparable with thermal modeling which suggests rates of 150 °C/min to produce highly glassy exteriors whereas microlite growth in the interior of the same clast occurs at 12 °C/min in basaltic scoria at Shishaldin volcano, in Alaska (Szramek et al. 2010). Measurements of bomb field emplacement from FLIR cameras at Stromboli measure cooling rates an order of magnitude slower, which may be due to the lower temperature of emplacement as the observed bombs cooled during flight (Harris et al. 2013; Vanderkluysen et al. 2012). The microlites of experimental clasts were smaller and more sparse than natural samples; however, indicating further work needs to be done.

Despite having similar cooling rates, the F value of the clasts in the Szramek et al. (2010) study was 0 compared with our experiments where F values range up to 64% (Table 3). Experimental clasts that contain microlites had longer time above glass transition temperature when compared with unfused scoria from another basaltic Shishaldin Volcano (t_g = 22–67 min compared with 3–21 min; Szramek et al. 2010), further suggesting that compared with interior cooling rate, t_g is more representative of the thermal conditions which effect fusion in a deposit. Despite having the same interior cooling rates, the difference in t_g is inferred to be due to the "eruption" temperature. Specifically, "eruption" temperature was significantly lower in the modeling calculation (1060 °C; Szramek et al. 2010) than in our experiments (~ 1200 °C).

Outer texture and color of clasts

The morphology and texture of the outer layer of the experimental clasts resembles the outside of natural clasts. Specifically, both exhibit brittle features such as tears (Fig. 8a), and both have ductile features, including stretched vesicles and small-scale folds or wrinkles. Virtually all clasts had an initial colorful, shiny coating on interior and exterior surfaces (Fig. 8b).

In natural deposits, red is a common color originating from oxidized iron in glass as well as oxidized hematite in weathered deposits (e.g., Mellors and Sparks 1991; Moriizumi et al. 2009; D'Oriano et al. 2013; Rader et al. 2018; Cottrell et al. 2018). Red is a rare color found in our in experiments (only observed in SLP16–15; Fig. 8) so perhaps the cooling rates observed here are too quick for the oxidation of iron in the glass or the formation of secondary oxidized hematite.

Colorful coatings have been described at several natural locations including Muana Ulu (Parcheta et al. 2013; Jones et al. 2018) and southern Idaho (Stearns 1924). Coloration of the Broken Top and Blue Dragon lava flows in Southern Idaho are proposed to be caused by electron transfer between Fe^{2+} and Fe^{3+} or Fe^{2+} and Ti^{4+} within the oxidized outer layer of the glass (Faye and Miller 1973). The colors of natural samples are less reflective/metallic looking when compared with experiments. The distribution of the colors also differs between experiments and natural samples. Unlike the Broken Top and Blue Dragon colorations, the sheen on the experimental clasts is strongest in regions of trapped volatiles including the inside of some vesicles. Despite the different locations of the color, the connection with H- and O-rich volatiles suggests that oxidation is likely an important formation

mechanism in the experiments. Previous experimental trials which had no gravel added were far less likely to have colorful coatings suggesting the added volatiles are important for the coloration as opposed to other factors in the methodology that were consistent between iterations of this method, such as interacting with the steel trough, paddle, or containers.

Conclusions

We have developed a method to create analog spatter deposits out of molten, basaltic rock, using the Syracuse Lava Project Facility. Our experiments successfully reproduced several morphological characteristics of natural spatter, including clast size, *F* value (degree of fusion between clasts), and coloration and provide temperature ranges in a manner that allowed for quantitative constrains on the thermal evolution of spatter deposits. Other characteristics were more challenging, including vesicularity, microcrystallinity, deposit void space, and aspect ratio, all of which be improved upon in future experiments. However, these characteristics still allowed for qualitative comparisons and their very presence pushed this model closer toward realistic conditions.

By tracking the thermal evolution of the experimental clasts, we identified minimum conditions for fusion. For basaltic clasts to fuse, accumulation rates must exceed 2 m/h, internal clast temperatures must be in excess of 900 °C, surface temperatures must achieve 850 °C, and the clasts must remain above the glass transition temperature for at least 30 min. Our experimental conditions correspond closely to those required for fusion determined in natural spatter deposits. Furthermore, our experiments indicate that the degree of fusion (*F* value) is dependent on the time clasts are in contact above the glass transition point, their initial temperature, and pressured applied to clasts: the longer clasts are in contact with each other above the glass transition temperature, the higher the connectivity between clasts.

Our experiments also support conclusions made by spatter population studies, which indicate that deposit morphology can be used to identify eruptive conditions in historical deposits (Rader et al. 2018; Jones et al. 2018). Additionally, accumulation rates of 2.5–4.5 m/h were estimated for Southern Idaho spatter features, suggesting higher rates are necessary to produce rheomorphic textures, induce collapse or produce a clastogenic flow.

Acknowledgements This study required the dedicated contributions of numerous undergraduate and graduate students from Syracuse University, Colgate University, and Franklin and Marshall College. The writing was greatly improved through discussions with Dr. John Wolff and E. Rader's writing group. Editing and suggestions by Ingo Sonder, Karoly Nemeth, two anonymous reviewers, and handling editor Laura Pioli, as well as Andrew Harris were extremely helpful and are deeply appreciated. A. Sehlke assisted with XRF analyses and a final thanks is owed to the Hawaiian Volcano Observatory, which secured access to the Leilani eruption site, allowing for the visual record of the height of spatter ramparts at fissure 11.

Funding information Funding for this study originates from several sources including the FINESSE project and the NASA Postdoctoral Program of the United Space Research Association, as well as several grants from Colgate University during the early stages of experimentation.

References

Berman DC, Hartmann WK (2002) Recent fluvial volcanic and tectonic activity on the Cerberus plains of Mars. Icarus 159:1–17

Capaccioni B, Cuccoli F (2005) Spatter and welded air fall deposits generated by fire-fountaining eruptions: cooling of pyroclasts during transport and deposition. J Volcanol Geotherm Res 145:263–280

Carling GT, Radebaugh J, Saito T, Lorenz RD, Dangerfield A, Tingey DG, Diniega S (2015) Temperatures thermal structure and behavior of eruptions at Kilauea and Erta Ale volcanoes using a consumer digital camcorder. Geo Res J 5:47–56

Carracedo Sanchez M, Sarrionandia F, Arostegui J, Eguiluz L, Gil Ibarguchi JI (2012) The transition of spatter to lava-like body in lava fountain deposits: features and examples from the Cabezo Segura volcano (Calatrava Spain). J Volcanol Geotherm Res 227:1–14

Cashman KV (1993) Relationship between plagioclase crystallization and cooling rate in basaltic melts. Contrib Mineral Petrol 113:126–142

Cashman KV, Mangan MT (1994) Physical aspects of magma degassing, II, Constraints on vesiculation processes from textural studies of eruptive products, Volatiles in Magmas MR Carroll, JR Holloway. Mineral. Soc. of Am., Washington, D.C., pp 446–478

Conte AM, Perinelli C, Trigila R (2006) Cooling kinetics experiments on different Stromboli lavas: effects on crystal morphologies and phases composition. J Volcanol Geotherm Res 155:179–200

Costantini L, Bonadonna C, Houghton BF, Wehrmann H (2009) New physical characterization of the Fontana lapilli basaltic Plinian eruption Nicaragua. Bull Volcanol 71:337–355

Cottrell E, Lanzirotti A, Mysen B, Birner S, Kelley KA, Botcharnikov R, Davis FA, Newville M (2018) A Mössbauer-based XANES calibration for hydrous basalt glasses reveals radiation-induced oxidation of Fe. Am Mineral 103:489–501

D'Oriano C, Pompilio M, Bertagnini A, Cioni R, Pichavant M (2013) Effects of experimental reheating of natural basaltic ash at different temperatures and redox conditions. Contrib Mineral Petrol 165:863–883

Dietterich HR, Cashman KV, Rust AC, Lev E (2015) Diverting lava flows in the lab. Nat Geosci 8:494–496

Edwards BR, Karson J, Wysocki R, Lev E, Bindeman I, Kueppers U (2013) Insights on lava–ice/snow interactions from large-scale basaltic melt experiments. Geol 41:851–854

Farrell J, Karson J, Soldati A, Wysocki R (2018) Multiple-generation folding and non-coaxial strain of lava crusts. Bull Volcanol 80:84. https://doi.org/10.1007/s00445-018-1258-5

Faye GH, Miller RM (1973) 'Blue Dragon' basalt from craters of the Moon National Monument Idaho Origin of Color. Am Miner 58:1048

Fodor E, Németh K (2015) Spatter Cone. In: Hargitai H, Kereszturi A (eds) Encyclopedia of Planetary Landforms. Springer, New York, pp 2028–2034

Ganci G, Harris AJ, Del Negro C, Guéhenneux Y, Cappello A, Labazuy P, Calvari S, Gouhier M (2012) A year of lava fountaining at Etna: volumes from SEVIRI. Geophys Res Lett 39:6

Gerlach TM, Graeber EJ (1985) Volatile budget of Kilauea volcano. Nat 313:273–277

Giordano D, Nichols AR, Dingwell DB (2005) Glass transition temperatures of natural hydrous melts: a relationship with shear viscosity and implications for the welding process. J Volcanol Geotherm Res 142:105–118

Grunder A, Russell JK (2005) Welding processes in volcanology: insights from field experimental and modeling studies. J Volcanol Geotherm Res 142:1–9

Grunder AL, Laporte D, Druitt TH (2005) Experimental and textural investigation of welding: effects of compaction sintering and vapor-phase crystallization in the rhyolitic Rattlesnake Tuff. J Volcanol Geotherm Res 142:89–104

Gurioli L, Colo L, Bollasina AJ, Harris AJ, Whittington A, Ripepe M (2014) Dynamics of Strombolian explosions: inferences from field and laboratory studies of erupted bombs from Stromboli volcano. J Geophys Res 119:319–345

Harris AJ, Allen JS (2008) One- two-and three-phase viscosity treatments for basaltic lava flows. J Geophys Res Solid Earth 113:B9. https://doi.org/10.1029/2007JB005035

Harris AJ, Delle Donne D, Dehn J, Ripepe M, Worden AK (2013) Volcanic plume and bomb field masses from thermal infrared camera imagery. Earth Planet Sci Lett 365:77–85

Hawaii Civil Defense Map (n.d.) https://www.google.com/maps/d/u/0/viewer?mid=1CvBhH9wEeztBrqYbsGDi4YjU1k1QH5AL&ll=19.464297929466742%2C-154.8846891180474&z=13 (accessed 4-24-2020)

Head JW III, Wilson L (1989) Basaltic pyroclastic eruptions: influence of gas-release patterns and volume fluxes on fountain structure and the formation of cinder cones spatter cones rootless flows lava ponds and lava flows. J Volcanol Geotherm Res 37:261–271

Helz RT, Banks NG, Heliker C, Neal CA, Wolfe EW (1995) Comparative geothermometry of recent Hawaiian eruptions. J Geophys Res 100:17637–17657

Herd RA, Pinkerton H (1997) Bubble coalescence in basaltic lava: its impact on the evolution of bubble populations. J Volcanol Geotherm Res 75:137–157

Hofmeister A M, Sehlke A, Avard G, Bollasina A J, Robert G, , Whittington A G (2016) Transport properties of glassy and molten lavas as a function of temperature and composition J Volcanol Geotherm Res 327 https://doi.org/10.1016/jjvolgeores201608015, 330, 348

Hon KE, Kauahikaua JI, Denlinger R, Mackay K (1994) Emplacement and inflation of pahoehoe sheet flows: observations and measurements of active lava flows on Kilauea Volcano, Hawaii. Geol Soc Am Bull 106:351–370

Hort M, Gardner JE (2000) Constraints on degassing of pumice clasts during Plinian volcanic eruptions based on model calculations. J Geophys Res 105:25981–26001

HVO eruption chronology website (n.d.) https://volcanoes.usgs.gov/volcanoes/kilauea/multimedia_chronology.html (accessed April 24th, 2020)

Jones TJ, Houghton BF, Llewellin EW, Parcheta CE, Höltgen L (2018) Spatter matters–distinguishing primary (eruptive) and secondary (non-eruptive) spatter deposits. Sci Rep 8:9179

Keszthelyi L (1994) Calculated effect of vesicles on the thermal properties of cooling basaltic lava flows. J Volcanol Geotherm Res 63: 257–266

Keszthelyi L, Denlinger R (1996) The initial cooling of pahoehoe flow lobes. Bull Volcanol 58:5–18

Koleszar AM, Rader E, Harpp KS (2018) The Saga of Volcville: a large-scale lava flow hazard mitigation exercise for undergraduates with the Syracuse Lava Project (SLP) In AGU Fall Meeting Abstracts

Kuntz MA, Champion DE, Spiker EC, Lefebvre RH, McBroome LA (1982) The great rift and the evolution of the craters of the moon lava field, Idaho. Cenozoic Geol Idaho: Idaho Bu Mines Geol Bull 26:423–437

Lautze NC, Houghton BF (2005) Physical mingling of magma and complex eruption dynamics in the shallow conduit at Stromboli volcano, Italy. Geol 33:425–428

Lesher CE, Cashman KV, Mayfield JD (1999) Kinetic controls on crystallization of Tertiary North Atlantic basalt and implications for the emplacement and cooling history of lava at site 989 Southeast Greenland rifted margin. In: Larsen HC, Duncan RA, Allan JF, Brooks K (eds) Proceedings of the Ocean Drilling Project Scientific Results, vol 163, pp 135–148

Lev E, Spiegelman M, Wysocki RJ, Karson JA (2012) Investigating lava flow rheology using video analysis and numerical flow models. J Volcanol Geotherm Res 247:62–73

Lev E, Rumpf E, Dietterich H (2019) Analog experiments of lava flow emplacement. Ann Geophys 62:225

Lofgren GE (1983) Effect of heterogeneous nucleation on basaltic textures: a dynamic crystallization study. J Petrol 24:229–255

Mader HM, Llewellin EW, Mueller SP (2013) The rheology of two-phase magmas: a review and analysis. J Volcanol Geotherm Res 257:135–158. https://doi.org/10.1016/jjvolgeores201302014

Manga M, Castro J, Cashman KV, Loewenberg M (1998) Rheology of bubble-bearing magmas. J Volcanol Geotherm Res 87(1–4):15–28

Mangan MT, Cashman KV (1996) The structure of basaltic scoria and reticulite and inferences for vesiculation foam formation and fragmentation in lava fountains. J Volcanol Geotherm Res 73:1–18

Manley CR (1996) In situ formation of welded tuff-like textures in the carapace of a voluminous silicic lava flow Owyhee County SW Idaho. Bull Volcanol 57:672–686

Mellors RA, Sparks RSJ (1991) Spatter-rich pyroclastic flow deposits on Santorini Greece. Bull Volcanol 53:327–342

Moriizumi M, Nakashima S, Okumura S, Yamanoi Y (2009) Color-change processes of a plinian pumice and experimental constraints of color-change kinetics in air of an obsidian. Bull Volcanol 71:1–13

Morrison AA, Whittington A, Smets B, Kervyn M, Sehlke A (2020) The rheology of crystallizing basaltic lavas from Nyiragongo and Nyamuragira volcanoes, DRC. Volcanica 9:1–28

Moufti M, Nemeth K, Murcia H, Lindsay J, El Masry N (2013) Geosite of a steep lava spatter cone of the 1256 AD Al Madinah eruption Kingdom of Saudi Arabia. Open Geosci 5:189–195

Mouginis-Mark PJ, Wilson L, Zuber MT (1992) The physical volcanology of Mars. Mars:424–452

Mueller S, Llewellin EW, Mader HM (2011) The effect of particle shape on suspension viscosity and implications for magmatic flows. Geophys Res Lett 38:13

Myers ML, Geist DJ, Rowe MC, Harpp KS, Wallace PJ, Dufek J (2014) Replenishment of volatile-rich mafic magma into a degassed chamber drives mixing and eruption of Tungurahua volcano. Bull Volcanol 76:872

Myers ML, Wallace PJ, Wilson CJ (2019) Inferring magma ascent timescales and reconstructing conduit processes in explosive rhyolitic eruptions using diffusive losses of hydrogen from melt inclusions. J Volcanol Geotherm Res 369:95–112

Oppenheimer C (1991) Lava flow cooling estimated from Landsat thematic mapper infrared data: the Lonquimay eruption (Chile, 1989). J Geophys Res 96:21865–21878

Parcheta CE, Houghton BF, Swanson DA (2012) Hawaiian fissure fountains 1: decoding deposits—episode 1 of the 1969–1974 Mauna Ulu eruption. Bull Volcanol 74:1729–1743

Parcheta CE, Houghton BF, Swanson DA (2013) Contrasting patterns of vesiculation in low intermediate and high Hawaiian fountains: a case study of the 1969 Mauna Ulu eruption. J Volcanol Geotherm Res 255:79–89

Patrick MR, Dehn J, Dean K (2004) Numerical modeling of lava flow cooling applied to the 1997 Okmok eruption: approach and analysis. J Geophys Res 109:B3

Patrick MR, Orr T, Wilson D, Dow D, Freeman R (2011) Cyclic spattering seismic tremor and surface fluctuation within a perched lava channel Kilauea. Volcano Bull Volcanol 73:639–653

Pinkerton H, James M, Jones A (2002) Surface temperature measurements of active lava flows on Kilauea volcano, Hawai′ i. J Volcanol Geotherm Res 113:159–176

Pioli L, Pistolesi M, Rosi M (2012) Explosive magma interaction revealed by physical and textural properties of basaltic scoria at Stromboli volcano. InAGU Fall Meeting Abstracts

Pyle DM (1989) The thickness volume and grainsize of tephra fall deposits. Bull Volcanol 51:1–15

Quane SL, Russell JK (2005) Welding: insights from high-temperature analogue experiments. J Volcanol Geotherm Res 142:67–87

Quane SL, Russell JK, Friedlander EA (2009) Time scales of compaction in volcanic systems. Geol 37:471–474

Rader E, Geist D (2015) Eruption conditions of spatter deposits. J Volcanol Geotherm Res 304:287–293

Rader E, Kobs-Nawotniak S, Heldmann J (2018) Variability of spatter morphology in pyroclastic deposits in southern Idaho as correlated to thermal conditions and eruptive environment. Earth Space Sci 5: 592–603

Reynolds P, Brown RJ, Thordarson T, Llewellin EW (2016) The architecture and shallow conduits of Laki-type pyroclastic cones: insights into a basaltic fissure eruption. Bull Volcanol 78:36

Robert B, Harris A, Gurioli L, Médard E, Sehlke A, Whittington A (2014) Textural and rheological evolution of basalt flowing down a lava channel. Bull Volcanol 76:824

Robertson EC, Peck DL (1974) Thermal conductivity of vesicular basalt from Hawaii. J Geophys Res 79:4875–4888

Rumpf ME, Lev E, Wysocki R (2018) The influence of topographic roughness on lava flow emplacement. Bull Volcanol 80(7):63

Russell JK, Quane SL (2005) Rheology of welding: inversion of field constraints. J Volcanol Geotherm Res 142:173–191

Rust AC, Manga M (2002) Effects of bubble deformation on the viscosity of dilute suspensions. J Non-Newtonian Fluid Mech 104:53–63

Schneider CA, Rasband WS, Eliceiri KW (2012) NIH Image to ImageJ: 25 years of image analysis. Nat Methods 9:671–675

Sehlke A, Whittington AG (2016) The viscosity of planetary tholeiitic melts: a configurational entropy model. Geochim Cosmochim Acta 191:277–299

Sehlke A, Whittington A, Robert B, Harris A, Gurioli L, Médard E (2014) Pahoehoe to aa transition of Hawaiian lavas: an experimental study. Bull Volcanol 76:876

Shea T, Houghton BF, Gurioli L, Cashman KV, Hammer JE, Hobden BJ (2010) Textural studies of vesicles in volcanic rocks: an integrated methodology. J Volcanol Geotherm Res 190:271–289

Soldati A, Sant CJ, Farrell JA, Karson J (2018) The Effect of Bubbles On The Rheology Of Lava Flows: Insights From Large-Scale Two-Phase Experiments. In AGU Fall Meeting Abstracts

Stearns HT (1924) Craters of the Moon National Monument. Geogr Rev 14:362–372

Stevenson RJ, Dingwell DB, Webb SL, Sharp TG (1996) Viscosity of microlite-bearing rhyolitic obsidians: an experimental study. Bull Volcanol 58:298–309

Stovall WK, Houghton BF, Hammer JE, Fagents SA, Swanson DA (2012) Vesiculation of high fountaining Hawaiian eruptions: episodes 15 and 16 of 1959 Kīlauea Iki. Bull Volcanol 74:441–455

Sumner JM (1998) Formation of clastogenic lava flows during fissure eruption and scoria cone collapse: the 1986 eruption of Izu-Oshima Volcano eastern Japan. Bull Volcanol 60:195–212

Sumner JM, Blake S, Matela RJ, Wolff JA (2005) Spatter. J Volcanol Geotherm Res 142:49–65

Szramek L, Gardner JE, Hort M (2010) Cooling-induced crystallization of microlite crystals in two basaltic pumice clasts. Am Mineral 95: 503–509

Taddeucci J, Scarlato P, Capponi A, Del Bello E, Cimarelli C, Palladino DM, Kueppers U (2012) High-speed imaging of Strombolian explosions: the ejection velocity of pyroclasts. Geophys Res Lett 39:2

Vanderkluysen L, Harris AJ, Kelfoun K, Bonadonna C, Ripepe M (2012) Bombs behaving badly: unexpected trajectories and cooling of volcanic projectiles. Bull Volcanol 74:1849–1858

Wadsworth FB, Vasseur J, von Aulock FW, Hess KU, Scheu B, Lavallée Y, Dingwell DB (2014) Nonisothermal viscous sintering of volcanic ash. J Geophys Res 119:8792–8804

Webb SL, Dingwell DB (1990) The onset of non-Newtonian rheology of silicate melts. Phys Chem Miner 17:125–132

Worden A, Dehn J, Ripepe M, Delle Donne D (2014) Frequency based detection and monitoring of small scale explosive activity by comparing satellite and ground based infrared observations at Stromboli Volcano, Italy. J Volcanol Geotherm Res 283:159–171